**Showcasing research from the CREATIS (Centre de Recherche en Acquisition et Traitement de l'Image pour la Santé), Claude Bernard University, Lyon, France.**

Evaluation of spectral photon counting computed tomography K-edge imaging for determination of gold nanoparticle biodistribution *in vivo*

Spectral photon counting computed tomography (SPCCT) is an emerging medical imaging technology that records the energy of incident photons allowing for the specific detection of contrast agents due to measurement of their characteristic X-ray attenuation profiles. This approach is known as K-edge imaging. Gold nanoparticles have been reported as potential contrast agents for SPCCT imaging. In this study, we have demonstrated the potential of the SPCCT imaging system for non-invasive quantitative determination of gold nanoparticle biodistribution *in vivo* over time, giving us confidence about the impact of SPCCT on nanoparticle development.

ROYAL SOCIETY OF **CHEMISTRY**

rsc.li/nanoscale

Nanoscale

Check for updates
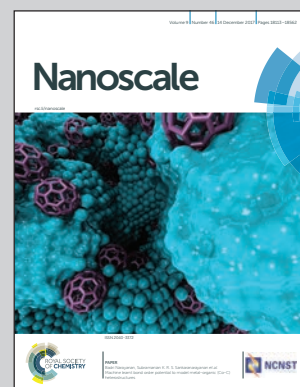
Evaluation of spectral photon counting computed tomography K-edge imaging for determination of gold nanoparticle biodistribution *in vivo*†

Salim Si-Mohamed, [ID] [a,b] David P. Cormode, [ID] [c] Daniel Bar-Ness,[b]
Monica Sigovan,[a,b] Pratap C. Naha, [ID] [c] Jean-Baptiste Langlois, [ID] [d]
Lara Chalabreysse,[e] Philippe Coulon,[f] Ira Blevis,[g] Ewald Roessl,[h] Klaus Erhard,[h]
Loic Boussel[a,b] and Philippe Douek*[a,b]

Spectral photon counting computed tomography (SPCCT) is an emerging medical imaging technology. SPCCT scanners record the energy of incident photons, which allows specific detection of contrast agents due to measurement of their characteristic X-ray attenuation profiles. This approach is known as K-edge imaging. Nanoparticles formed from elements such as gold, bismuth or ytterbium have been reported as potential contrast agents for SPCCT imaging. Furthermore, gold nanoparticles have many applications in medicine, such as adjuvants for radiotherapy and photothermal ablation. In particular, longitudinal imaging of the biodistribution of nanoparticles would be highly attractive for their clinical translation. We therefore studied the capabilities of a novel SPCCT scanner to quantify the biodistribution of gold nanoparticles *in vivo*. PEGylated gold nanoparticles were used. Phantom imaging showed that concentrations measured on gold images correlated well with known concentrations (slope = 0.94, intercept = 0.18, RMSE = 0.18, R^2 = 0.99). The SPCCT system allowed repetitive and quick acquisitions *in vivo*, and follow-up of changes in the AuNP biodistribution over time. Measurements performed on gold images correlated with the inductively coupled plasma-optical emission spectrometry (ICP-OES) measurements in the organs of interest (slope = 0.77, intercept = 0.47, RMSE = 0.72, R^2 = 0.93). TEM results were in agreement with the imaging and ICP-OES in that much higher concentrations of AuNPs were observed in the liver, spleen, bone marrow and lymph nodes (mainly in macrophages). In conclusion, we found that SPCCT can be used for repetitive and non-invasive determination of the biodistribution of gold nanoparticles *in vivo*.

Introduction

Since its introduction in the early 1970s, computed tomography (CT) has become the workhorse of diagnostic imaging

[a]*Radiology Department, Centre Hospitalier Universitaire, Lyon, France.*
E-mail: douek@creatis.insa-lyon.fr; Tel: +0616597163
[b]*CREATIS, UMR CNRS 5220, Inserm U1044, University Lyon1 Claude Bernard, Lyon, France*
[c]*University of Pennsylvania, Department of Radiology, Philadelphia, PA, USA*
[d]*CERMEP-Imagerie du vivant, Lyon, France*
[e]*Centre Hospitalier Universitaire, Pathology Department, Lyon, France*
[f]*CT Clinical Science, Philips, Suresnes, France*
[g]*Philips, Global Advanced Technologies, CT, Haifa, Israel*
[h]*Philips GmbH Innovative Technologies, Research Laboratories, Hamburg, Germany*
†Electronic supplementary information (ESI) available: A table with the organ gold content, as determined from SPCCT image analysis. Transmission electron micrographs of the heart, kidney and brain. See DOI: 10.1039/c7nr01153a

owing to its cost effectiveness, wide availability, high spatial resolution, high temporal resolution, and diagnostic benefits. A current major area of research in CT is the use of photon counting detectors, referred to as spectral photon-counting CT (SPCCT), or as multicolor CT.[1–4] The photon-counting detectors are able to measure the energy of individual photons transmitted through the subject based on pulse height analysis, and allocate this information between multiple energy thresholds, called bins, leading to energy-based attenuation profiles of tissue.[3] One of the strengths of SPCCT is its ability to specifically detect exogenous contrast media. This is possible due to edges in the X-ray attenuation profiles of elements such as gold, which have their K-edge binding energy in the relevant energy range of the X-ray spectrum (K-edge energy of gold is 80.7 keV). This approach is known as K-edge imaging and eliminates the need for imaging before and after injection, since the location of the contrast media can be determined

solely from post-injection scan, streamlining the imaging and image analysis process. For instance, de Vries *et al.* investigated the feasibility and the accuracy of a small animal SPCCT scanner to determine the concentration and localization of iodine-based contrast agents in mice.[5]

Clinical computed tomography relies on the use of iodinated contrast agents. However, these iodinated agents have a number of limitations. Some patients are hypersensitive to iodinated agents.[6] These agents are contra-indicated for use in patients with renal insufficiency, as their use in such patients can lead to further reduction in kidney function, an event known as contrast-induced nephropathy.[7] Moreover, they are non-specific with diffused interstitial distribution and suffer from short imaging windows due to rapid renal clearance. Finally, the K-edge energy of iodine, 33.2 keV, is too low to be detected with clinical SPCCT systems, because of low X-ray flux at that point in the energy spectrum caused by high absorption in patients. Thus there is a compelling need to develop novel contrast agents for use with SPCCT.

Meanwhile, the field of nanoparticle contrast agents for CT has expanded rapidly over the past decade. Nanoparticles based on heavy elements, such as gold nanoparticles (AuNPs), can overcome the drawbacks of small molecule iodinated CT contrast agents.[8–13] Several groups have demonstrated AuNPs to be highly effective X-ray contrast agents, producing stronger contrast than iodinated agents, possessing the potential to circulate longer than iodinated contrast agents for improved blood pool imaging and possessing high biocompatibility.[9,12,14–16] In addition, gold nanoparticles have been shown to be potent contrast agents for SPCCT[17] and have been shown to be effective imaging agents for the characterization of atherosclerosis with a preclinical system.[18] Moreover, gold nanoparticles and nanoparticles based on other heavy elements have been employed in a plethora of biomedical applications such as adjuvants for radiotherapy, photothermal ablation, drug delivery, photoacoustics, surface enhanced Raman imaging and others.[19] Methods that would allow the non-invasive assessment of the biodistribution of such agents at multiple time points would be highly valuable.

SPCCT has the potential to track the biodistribution and elimination of heavy element based agents over time *via* repeated scanning, sparing the need to sacrifice animals at each time point to perform *ex vivo* analyses or to perform radiolabeling. However, to the best of our knowledge, studying the biodistribution of agents over extended timeframes with SPCCT has not been previously reported. This was due to the limitations of early SPCCT systems, such as very long scan times[5] that prevented *in vivo* image acquisitions. The SPCCT systems have now been developed with image acquisition times of 1 second that allow dynamic and repetitive imaging *in vivo*, such as a small field of view (FOV) SPCCT prototype system derived from a modified clinical CT system.[4]

The purpose of this study was to investigate the feasibility of SPCCT for specific characterization and quantification of a gold nanoparticle contrast agent's organ biodistribution *in vivo* over time.

Results and discussion

### Nanoparticle preparation and characterization

AuNPs were prepared from reduction of gold chloride with sodium citrate in boiling water, and then capped with thiol-PEG-2000. This process yielded gold nanoparticles (Fig. 1A) with a core size of 12.5 nm as found from transmission electron microscopy (TEM) (Fig. 1B) and a mean hydrodynamic diameter of 18 nm as determined by dynamic light scattering (DLS). The concentration of the gold solution was determined from inductively coupled plasma-optical emission spectroscopy (ICP-OES) to be 65 mg ml^{-1}. The pH was the same as that of iopamidol and phosphate buffered saline (PBS) solutions (7.46 ± 0.05). The viscosity of an X-ray contrast agent needs to be low to allow rapid injection and avoid adverse side effects.[20] We therefore measured the viscosity of the AuNPs. The dynamic viscosity of the gold nanoparticles was lower than that of iopamidol, being 1.14 ± 0.03 mPa s^{-1} and 1.28 ± 0.18 mPa s^{-1} respectively, indicating that the gold nanoparticles have good viscosity for *in vivo* applications.

SPCCT phantom imaging

We performed phantom imaging experiments to test the specific material discrimination capabilities of this SPCCT prototype. The images of the phantom provided by the SPCCT system are conventional CT images, water material decomposition images and gold images (Fig. 2B). As can be seen, the scanner could specifically detect and accurately quantify the range of concentrations of AuNPs, with a very good linear correlation between the concentrations measured on the gold images and the concentrations prepared having a slope close to 1 (slope = 0.94, intercept = 0.17, R^2 = 0.99, RMSE = 0.18), and good agreement with a bias of 0.11 demonstrated by the Bland–Altman analysis (Fig. 2C and D). The PBS in the tubes is seen in the water images, as is the plastic of the phantom and the tubes, since it has a similar X-ray attenuation profile to water.

In vivo SPCCT imaging

New Zealand white rabbits were injected with AuNPs without any obvious side effects and scanned three times on the day of
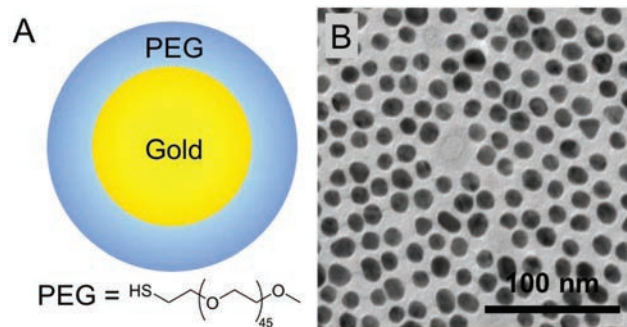
Fig. 1 (A) Schematic representation of the AuNP. (B) Transmission electron micrograph of the AuNP.
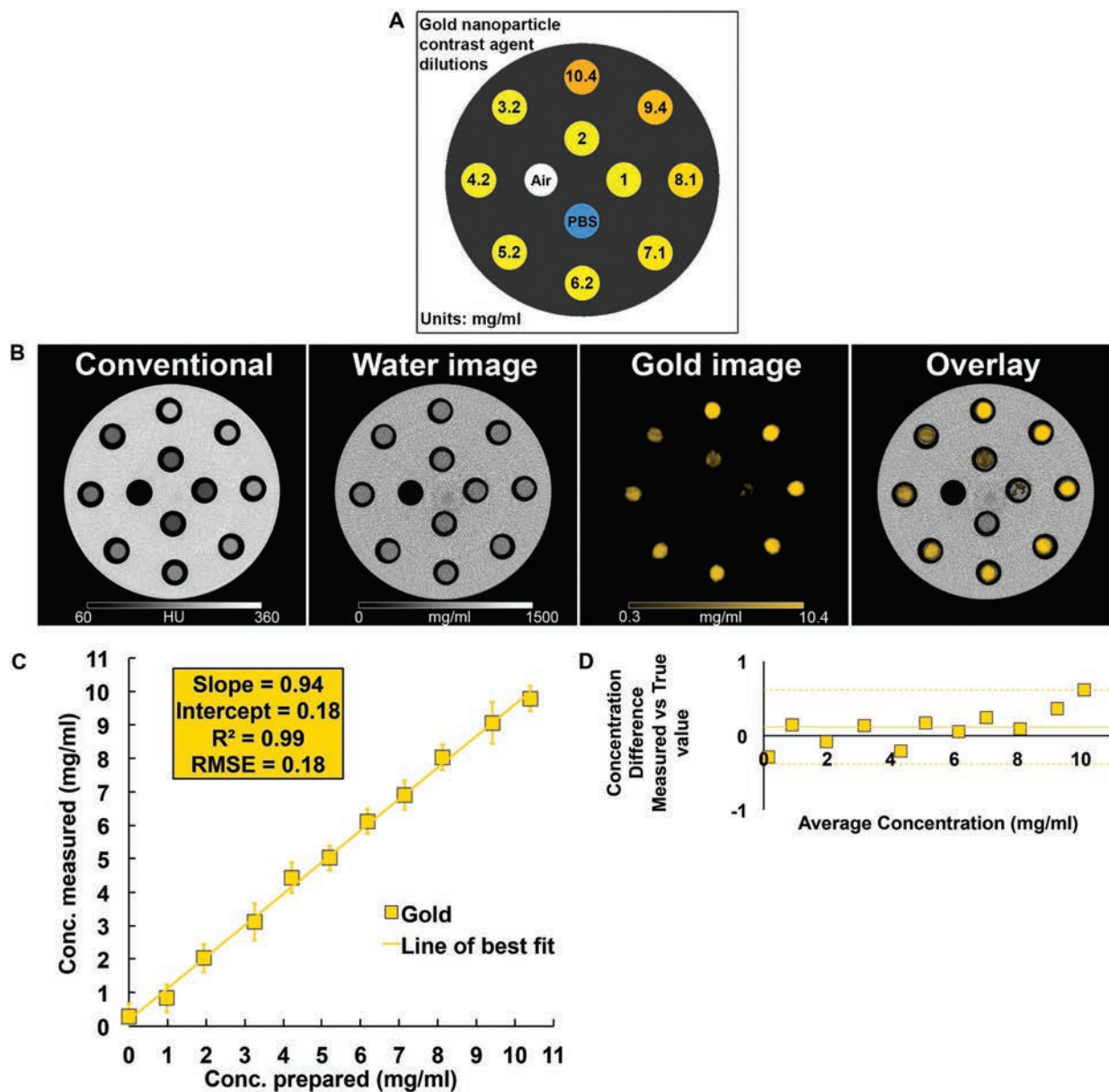
Fig. 2 (A) Diagram of the phantom used. (B) SPCCT derived images (left to right: conventional CT image, water material decomposition, gold image and overlay of gold image on water image). (C) Comparison between the expected and measured concentrations. (D) Bland–Altman plot depicting the comparison of gold content between the prepared and measured concentration as determined by SPCCT image analysis.

injection (once pre- (T0) and twice post-injection (T1 and T2)). They were also scanned at one week (W1), one month (M1) and six months (M6) post-injection in order to determine and quantify the biodistribution of the contrast agent. The contrast agent was chosen because its K-edge is at 80.7 keV, relatively close to the effective energy of the X-ray spectrum used (30–120 keV). Furthermore, these AuNPs have long circulation times permitted by the hydrodynamic diameter of 18 nm and the thiol-PEG coating.[9] Also, there is widespread interest in the use of gold nanoparticles in an array of diagnostic and therapeutic applications.[21–25]

The SPCCT system allowed us to perform repetitive imaging *in vivo* with 1-second acquisition time and provided conven-

tional CT and quantitative gold images (Fig. 3–6). The gold images allowed specific detection of gold nanoparticles in the organs of interest and showed differential temporal uptake between organs (Fig. 3 and 6). For example, AuNPs were highly concentrated in blood at 8 min post injection (4.76 ± 0.51 mg ml^{-1}), but negligible values were found at one week and one month post-injection (0.16 ± 0.42 mg ml^{-1}), matching the expected blood pool pharmacokinetics.[9] On the other hand, the gold content in the liver, spleen, and bone marrow, was lower at T1 and T2 (the gold content at these time points is likely due to AuNPs in the blood perfusing the organs) with persistent higher concentrations in scans acquired at 1 week, 1 month and 6 months (Fig. 3–6). At the last time point, the
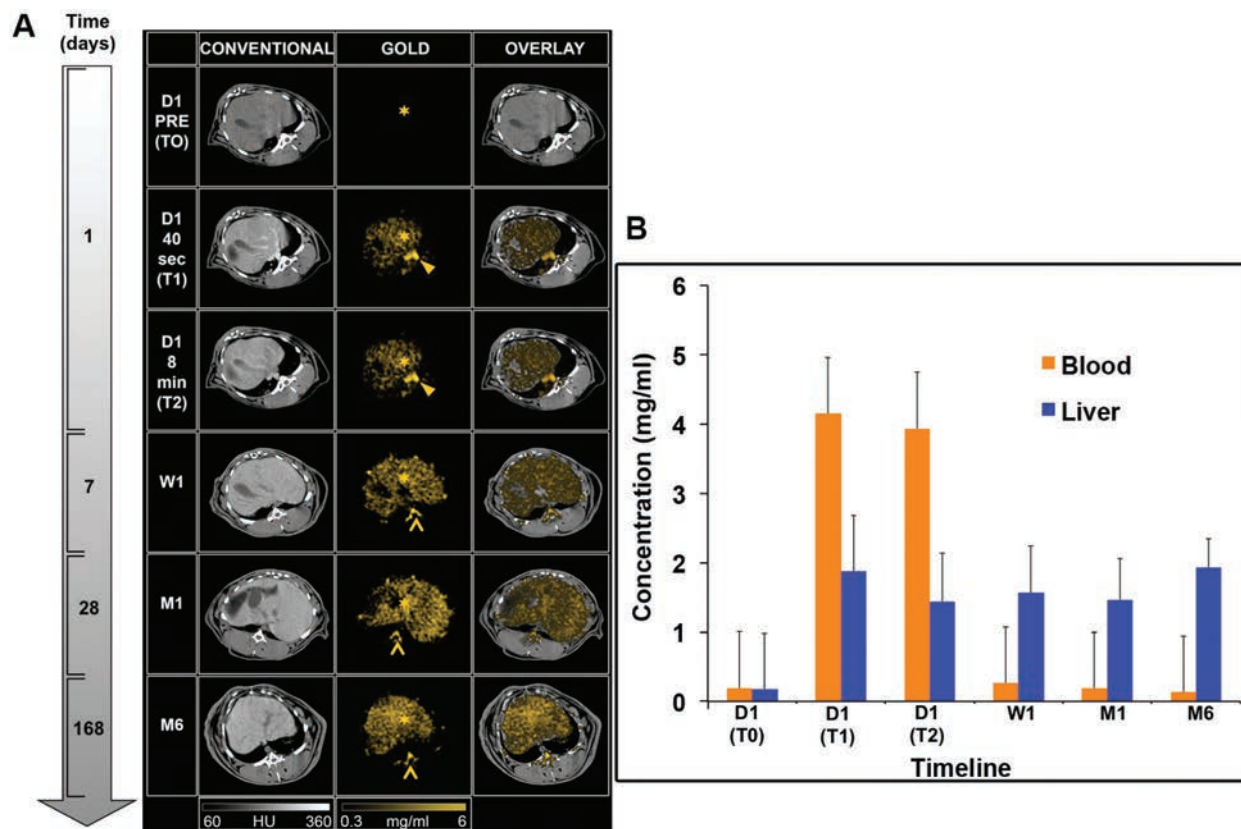
Fig. 3 (A) SPCCT images displaying the AuNP biodistribution in the liver over time (left to right: conventional CT image, gold image and overlay). Star: liver, arrowhead: aorta, chevron: bone marrow. (B) Gold content in the liver and blood at various time points, as determined from SPCCT image analysis.

SPCCT system was used to perform a helical scan that covered the entire body of the animal (Fig. 5). This whole body scan revealed lymph nodes that contained gold with a concentration in the same range as the spleen. The liver, spleen and bone marrow are part of the mononuclear phagocyte system (MPS), and had sustained gold uptake and retention over time (Fig. 6). The gold content observed in the muscle and brain was close to zero at all time points, which is as expected since the nanoparticles are too large to extravasate in these organs. In the kidney and the urinary cavity, about 2 mg ml^{-1} of gold was detected at T1 and T2 without any signal at follow-up. A table with the gold concentrations in the organs, as determined from image analysis is presented in the ESI.†

Ex vivo analysis

In order to determine whether the measurements acquired from the SPCCT system were accurate, we sacrificed the animals (2 animals at 6 months, 2 animals at 1 month, 1 animal at one week) and performed ICP-OES on the organs ($n = 25$). Comparison between concentrations measured with SPCCT and ICP-OES showed a linear correlation between the two measurements ($R^2 = 0.93$, intercept = 0.47, RMSE = 0.77) (Fig. 7A), and agreement with a bias of 0.11 demonstrated by the Bland–Altman analysis (Fig. 7B). SPCCT underestimated the gold con-

centration in the organs by 23% on average with an offset of 0.47, compared to ICP-OES values, however, this indicates quite good accuracy (Fig. 7A). Moreover, the data indicates that the highest concentration of AuNPs is in the spleen.

Furthermore, to probe the localization of AuNPs in organs, we performed TEM on tissues excised from the animals at the 6 month time point. We found the AuNPs in these tissues to be intact and of similar size to those injected. We mostly observed AuNPs aggregated inside lysosomes within macrophages in the organs of the MPS, *i.e.* liver, spleen, bone marrow and lymph nodes (Fig. 8A–L). AuNPs were absent in cardiac and brain tissues (Fig. S1A–F†). Moreover, surprisingly, we observed small amounts of AuNPs in the renal mesangial cells behind the glomerular membrane (Fig. S1G–I†).

In this study, we demonstrated that a small FOV spectral photon-counting computed tomography prototype system derived from a modified clinical CT system enables repeated, non-invasive quantitative biodistribution analysis of AuNPs *in vivo* with good accuracy compared to ICP-OES. We also demonstrated the ability of the SPCCT system to detect and quantify AuNPs that accumulated in the MPS.

In SPCCT, the transmitted spectrum is collected by photon-counting detectors that have the ability to respond individually
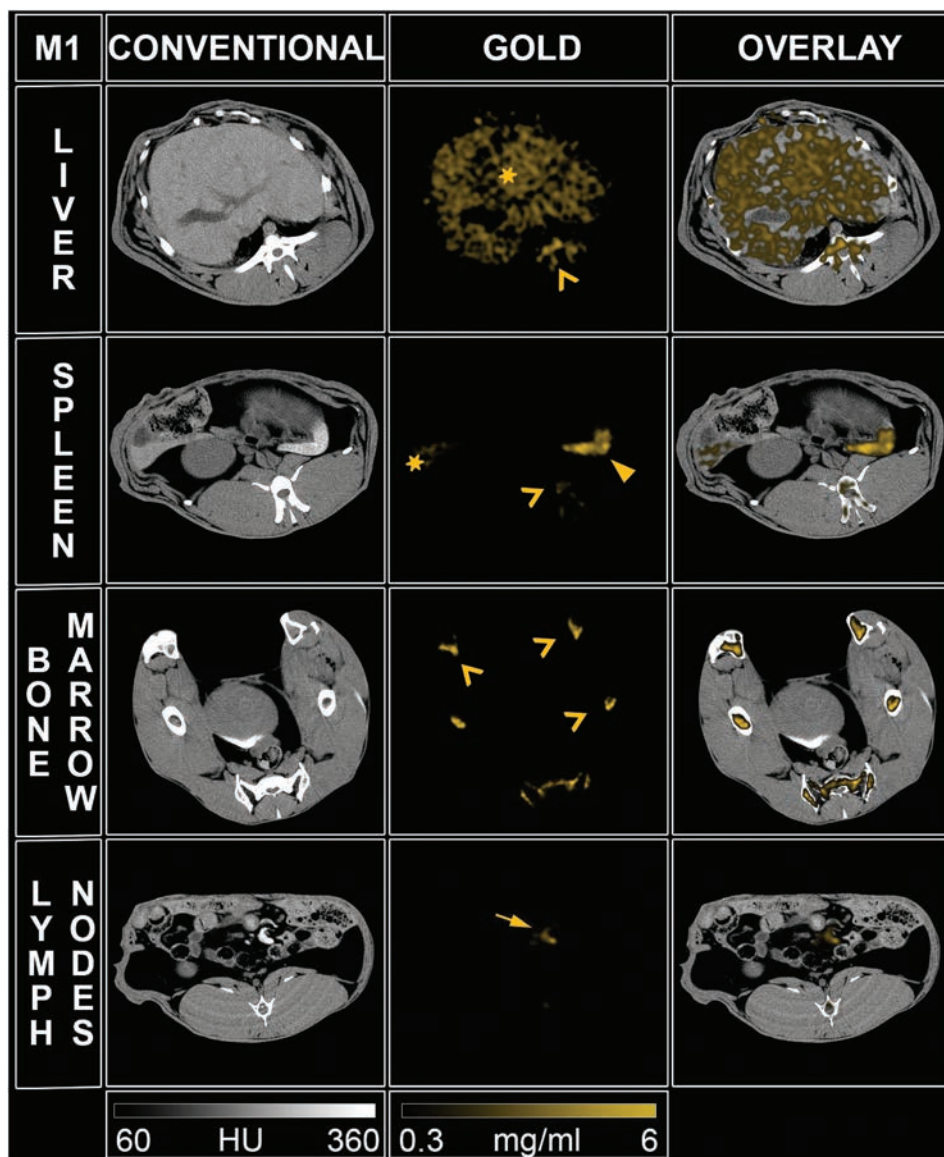
Fig. 4 SPCCT images displaying the AuNP retention at one month (M1) in the organs of the mononuclear phagocyte system (left to right: conventional CT image, gold image and overlay). Star: liver, head arrow: spleen, chevron: bone marrow, full arrow: lymph node.

to every single photon received and discriminate their energy.[26,27] The photons are divided into multiple different energy windows, referred to as bins, for which one or more boundaries can be adjusted to match the K-edge of the contrast agent studied, the K-edge being the binding energy of the K shell electron of an atom.[3,28–30] The limitation of the previous SPCCT systems was their lengthy scan times, which were as much as 24 hours for whole body imaging of a mouse.[31] This was due to the low photon flux needed to avoid pulse pileup in the detectors and limited number of detector rows. The small FOV SPCCT prototype scanner used for this study is equipped with detectors that have high flux capacity allowing high temporal resolution (1–1.5 seconds) compared to the previously reported prototypes,[32] allowing for the dynamic and repetitive imaging *in vivo* reported herein.[33]

Several advantages of using SPCCT for gold imaging have been highlighted in this study. First, the detection of AuNPs in the bone marrow is remarkable, since contrast arising in that tissue would likely have gone unnoticed or be undetectable on conventional images due to the nearby presence of bone, although the accuracy of detection in the bone marrow is not as good as for other organs as can be seen in Fig. 7, which may be due to factors such as beam hardening.[34] This highlights the strength of SPCCT, *i.e.* detection of contrast materials close to calcified structures. Moreover, a good linear correlation in phantom imaging between SPCCT and prepared concentrations, and *in vivo* imaging between ICP-OES and SPCCT derived concentrations has been demonstrated, indicating that SPCCT is a non-invasive quantitative imaging technique.[5,28,35] This capacity is promising as a new tool for asses-
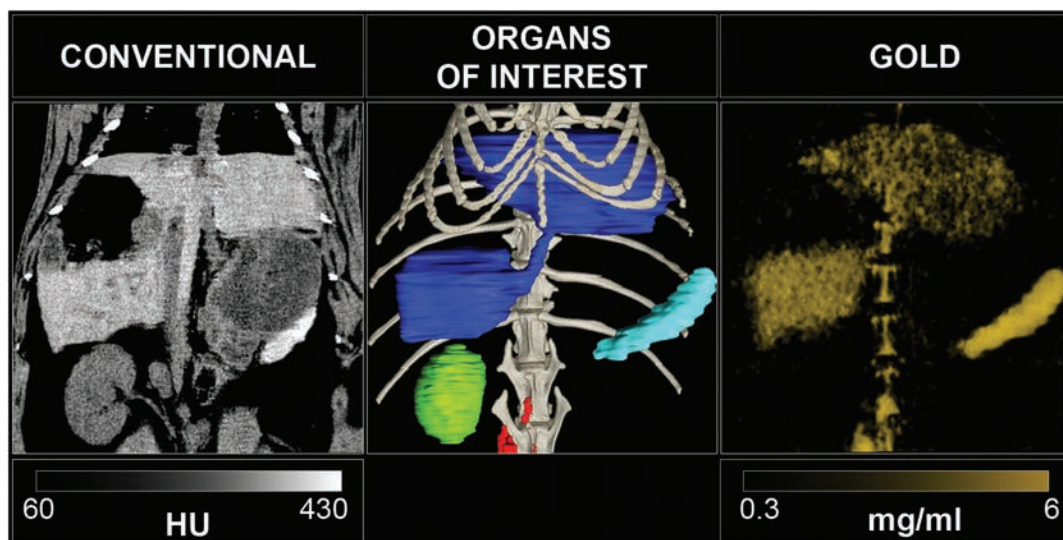
Fig. 5 Left: Abdomen SPCCT images of a rabbit at 6 months after injection of gold nanoparticles with the coronal conventional CT image, center: 3D volume rendering reconstruction of the conventional HU images with segmentation of the organs of interest (dark blue: liver, light blue: spleen, green: right kidney, red: lymph nodes, light grey: bone structure), right: 3D volume rendering reconstruction of the gold images.

sing non-invasively the biodistribution of materials that have a K-edge between ~40–100 keV, as opposed to ICP-OES based approaches, in which multiple groups of animals have to be sacrificed in a serial fashion and their organs dissected to obtain the biodistribution of contrast media at different time points. In addition, K-edge images benefit from the high spatial resolution provided by the photon-counting detectors as well as for the conventional CT images.[26] Finally, the added value provided by the multi bin photon-counting data is to provide both anatomical information from conventional CT images and specific information from material decomposition images simultaneously, allowing tracking of a targeted heavy element for functional information. Some of the competing techniques requiring two scans can suffer from motion between the acquisitions and therefore image registration issues,[36] and expose the subject to higher radiation dose.

Gold nanoparticles are being explored in many applications in the biomedical field such as contrast agents for medical imaging,[11,14] drug delivery, targeted killing of cells[21] and also therapeutic applications, such as theranostic agents[37] and radiosensitization.[38] This has led to numerous investigations of their toxicity and biodistribution. Previously, Naha *et al.*[12] have shown good cytocompatibility *in vitro* for these AuNPs, with no effect on cell cytoskeleton or cell spreading.

In vivo, we confirmed the blood pool effect of the AuNPs with a scant change in blood concentration between scans acquired immediately after injection and acquired at 8 minutes post injection. Indeed, the gold nanoparticles are designed for long lasting vascular phase CT imaging, and are referred to as a blood pool contrast agent. They are designed to be biocompatible without toxicity at very high concentrations, as Cai *et al.* showed in mice,[9] due to the PEG coating that increases its circulation half-life and reduces interactions with serum proteins. As they are 18 nm in diameter, theoreti-

cally no renal excretion was expected.[39] While some gold signals were observed in the renal pelvis, ICP and UV/vis analysis of urine did not indicate the presence of any AuNPs. Therefore the signal in the renal pelvis is likely due to AuNPs in the blood in this tissue.

Retention of AuNPs over time was demonstrated in organs of MPS, *e.g.* the bone marrow, the liver, and the spleen, confirmed by the TEM of these tissues, which revealed retention in the macrophages. These findings supported the results of Naha *et al.*[12] that typically observed macrophages to be more sensitive to AuNPs as compared to epithelial and fibroblast cells, likely due to their higher phagocytic activity and thus higher uptake of nanoparticles. Thus we corroborated the results of Cai *et al.*[9] who demonstrated that AuNPs are taken up by the MPS organs.

Moreover, retention of AuNPs at six months is consistent with the life span of tissue macrophages, which is several months or years, as also reported by others.[9,40] Finally, we noticed retention in the mesenteric lymph nodes *via* hyperintensities that appeared in the gold images, but would likely not have been noticed on conventional CT images. In summary, our study of biodistribution kinetics of these AuNPs demonstrated a biphasic clearance of the nanoparticles, *i.e.* a steady state of the agent in the blood compartment after injection and a subsequent slow clearance of the dose into the organs of the MPS, indicating poor biological elimination leading to potential concerns over long-term safety, although Hainfeld *et al.* did not find any evidence of toxicity in mice over one year.[41]

These findings emphasize the potential of SPCCT for mapping specific tissues due to their uptake of a contrast agent within a clinically significant range of sensitivity and detection threshold (1 mg ml^{-1}), similar to previous publications using dual energy CT[13] and spectral CT.[42] This capability should be
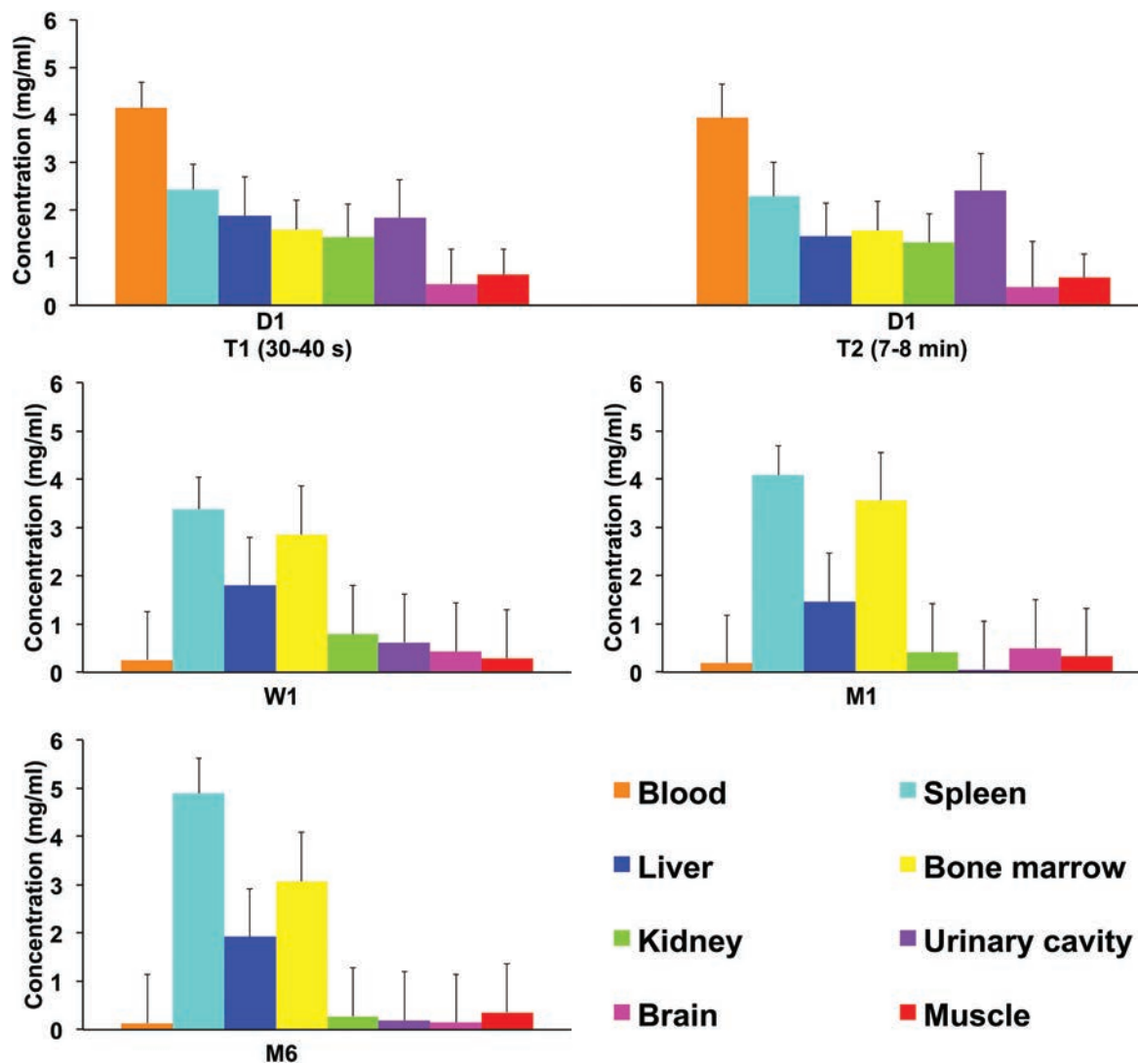
Fig. 6 The biodistribution of AuNP among the organs of interest at several time points. Error bars represent the mean of the noise in the ROIs.
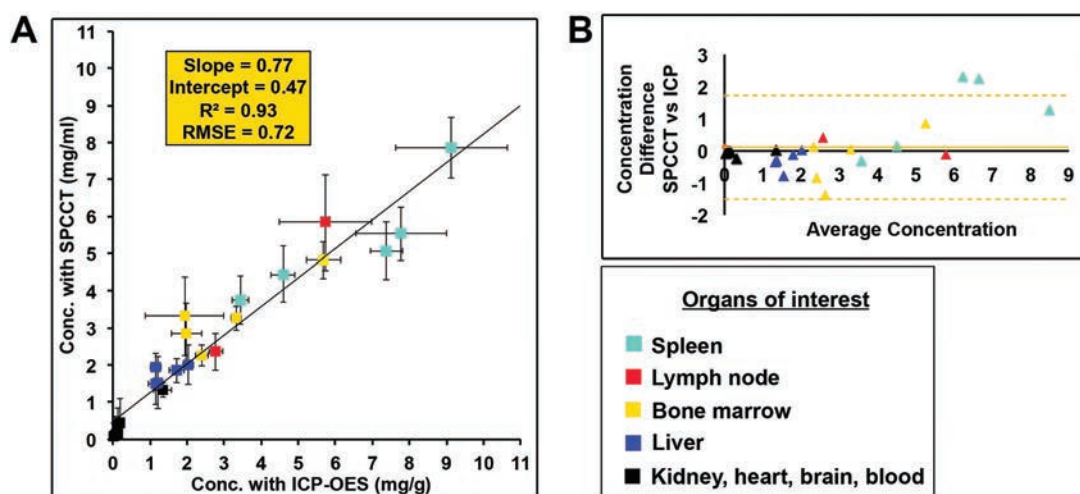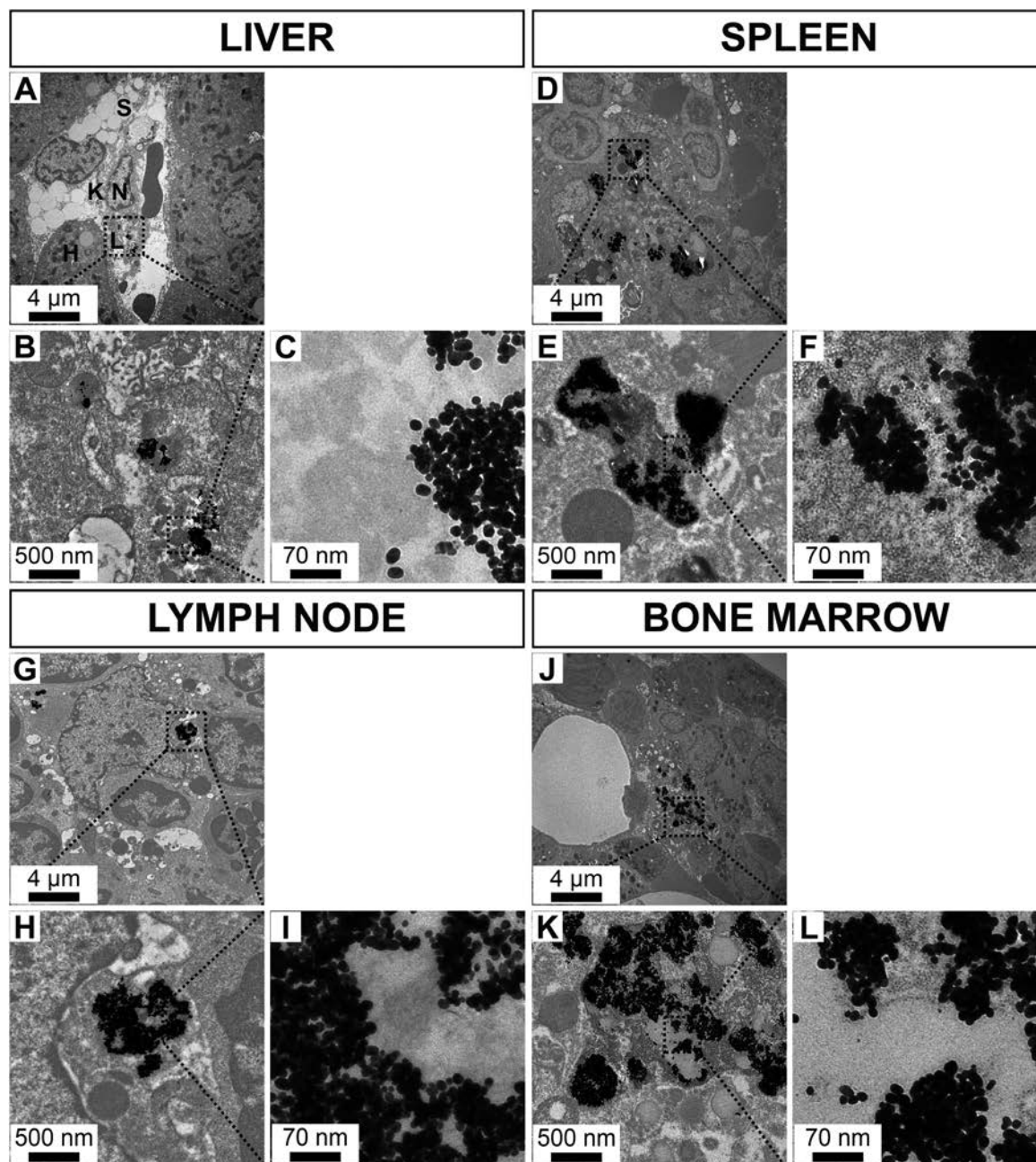

Fig. 7 (A) Comparison between the expected and measured concentrations. (B) Bland–Altman plot depicting the comparison of gold content in rabbit organs as determined *via* ICP-OES and SPCCT image analysis.

Fig. 8 Transmission electron micrographs of rabbit organs from the mononuclear phagocyte system 6 months after AuNP injection over a range of magnifications. A–C: Liver, D–F: spleen, G–I: lymph node, J–L: bone marrow (H: hepatocyte, K: Kupffer cell, L: lysosome, N: nucleus, S: sinusoid).

used for diagnosing pathological conditions with a differing uptake of the contrast agent. Indeed, this diagnostic approach is known and has already been used clinically, *i.e.* for localization of the sentinel lymph nodes in breast cancer with MRI *via* the use of iron oxide nanoparticles that are not taken up by pathologic lymph nodes[43] or imaging of the biliary tract *via* the use of an MRI-specific gadolinium contrast agent that is not excreted in the case of biliary cancer.[44] Compared to other techniques such as MRI or nuclear imaging, the strengths of SPCCT for this type of application would be its high temporal and spatial resolution, as well as whole-body imaging capabilities.

Moreover, SPCCT, as a pragmatic non-invasive tool for determining quantitative biodistribution *in vivo* over time, may be advantageous for use in the developing field of nanotechnology, which frequently uses heavy elements such as gold, bismuth, ytterbium and tantalum.[8,27,45–47]

Quantification of gold using ICP-OES was only performed at late time points. At these time points, significant quantities of gold were only found in the MPS organs, therefore the accuracy of the system was not tested in blood, muscle or brain. However, physics suggests that the system should be accurate for those tissues as well. We only compared ICP-OES to SPCCT

for a limited number of animals, *i.e.* n = 5, although the total number of organs compared was 25. The scanner used currently has a small field of view and z-coverage, limiting its ability to perform rapid, whole body imaging. Only five animals were used for the *in vivo* imaging, limiting statistical power. In addition, we did not study human subjects, for whom results may vary compared to this relatively small animal model, as the X-ray attenuation of humans will be greater. Finally, we have only studied gold based agents in this report, while agents based on bismuth, tantalum, ytterbium and other elements have been reported as CT contrast agents and for other applications.[10,47–51]

Conclusions

In summary, we have demonstrated the potential of the newly developed small FOV SPCCT prototype imaging system for the non-invasive quantitative determination of gold nanoparticle biodistribution *in vivo* over time, giving us confidence about the impact of SPCCT on nanoparticle development. Moreover, we have shown that the AuNPs used in this study are effective contrast agents for the vascular system initially and for the MPS over time, providing potential applications in the field of cardiovascular disease and cancer.

Experimental

SPCCT system

The SPCCT scanner (Philips Healthcare, Haifa, Israel) is a modified clinical base prototype that has a small field-of-view (FOV) of 168 mm in-plane and 2 mm z coverage, equipped with a conventional X-ray tube. Energies below 30 keV are filtered by pre-patient collimation and not transmitted, such as with a conventional clinical CT system. The photon-counting detectors are energy-sensitive detectors that have 5 rate counters with 5 different configurable energy thresholds.[52] For this study, the energy bins were set to 30–53, 53–78, 78–83, 83–98 and 98–120 keV in order to benefit from high differential sensitivity to materials with differing atomic numbers, and in particular from the K-edge absorption of gold (80.7 keV). A full description of the SPCCT system can be found elsewhere. Axial acquisitions were performed at 100 mA and 120 kVp with a gantry rotation time of 1 s and 2400 projections per rotation for the phantom and animal experiments. One additional helical acquisition was performed at the last time point to visualize whole body nanoparticle uptake.

SPCCT images

Multi-bin photon-counting data were pre-processed and a conventional CT image was derived from the information contained in all energy bins using a proprietary algorithm, corresponding to sum counts prior to reconstruction. After pile-up correction, material decomposition images were derived from the multi-bin photon-counting data and included a maximum-

likelihood based material decomposition of the attenuation into water, iodine and gold material bases.[3,33] The iodine images were formed as part of the standard reconstruction protocol, but were not analyzed as no iodine contrast agent injection was done. The resulting gold and water images are displayed in units mg ml^{-1}. Note that the gold images are K-edge images since they are formed from information derived from bins placed around the K-edge of gold. Images were reconstructed on a voxel grid of 0.25 × 0.25 × 0.25 mm^3 using conventional filtered back-projection without further post-processing besides removal of ring artifacts and utilization of a 2 pixel sigma Gaussian filter. For the analysis, the gold and water images were averaged to a slice thickness of 2 mm. For the representation of the organs of interest in Fig. 7, segmentation was done on the conventional images, while bone delineation was performed using windowing thresholds. No segmentation for the gold images was performed because of the specificity of the gold signal based on the gold images.

Gold nanoparticle preparation and characterization

Gold nanoparticles were synthesized, based on the previously reported methods.[12,53] The cores were formed by reducing gold chloride *via* addition of sodium citrate while at boiling point. Methoxy-PEG-2000-thiol was used to coat the resulting gold nanoparticles. The nanoparticles were washed three times with phosphate-buffered saline (PBS), concentrated and sterilized *via* syringe filtration. Samples of the final product were characterized by transmission electron microscopy (TEM) using a JEOL 1010 microscope, dynamic light scattering (DLS) using a Malvern Instruments Nano ZS 90 and inductively coupled plasma-optical emission spectroscopy (ICP-OES) using a Spectro Genesis system. The dynamic viscosity and the pH were also evaluated and compared to an iodinated contrast agent, iopamidol (65 mg ml^{-1}), and PBS. Viscosity was measured using a RFS3 rheometer from TA Instruments (New Castle DE). A pH meter was used.

Phantom imaging

In order to validate the quantification of gold using K-edge information, a cylindrical phantom of 15 cm diameter and made of acetal homopolymer was used. Ten 1.5 ml polypropylene centrifuge tubes, 1 cm in diameter, were filled with AuNP samples ranging in concentration from 1 to 10.4 mg ml^{-1}, diluted with PBS, and one was only filled with PBS. The design of the phantom is schematically depicted in Fig. 2A.

Animal experiments

Experiments were conducted with approval from the Institutional Animal Care and Use Committee (Council Directive No. 2010/63/UE on the protection of animals used for scientific purpose) under authorization number APAFIS#1732-2015091411181645v3. Five New Zealand white rabbits (Charles River, Canada, mean weight, 3.1 ± 0.5 kg; 2 females, 3 males; mean age, 7.4 ± 2.7 months) were anesthetized with 0.25 mg kg^{-1} intramuscular injection of médétomidine (1.0 mg ml^{-1}, Orion Pharma, Orion Corporation, Espoo, Finland) and

20 mg kg^{-1} intramuscular injection of ketamine (10.0 mg ml^{-1}, Merial, Lyon, France). 22-Gauge auricular vein catheters were placed. A veterinary handheld pulse oximeter and carbon dioxide detector (Model 9847 V, Nonin Medical, Inc, Plymouth, Minnesota) with a remote sensor pulse placed on the earlobe were used to monitor heart beat and oxygen saturation. Rabbits are the smallest animal model whose blood vessels are practical to image with a clinical scanner and have the benefit that the doses of contrast agents that need to be synthesized are relatively low compared with a larger animal model such as a pig.

3.5 ml kg^{-1} (about 12 ml) of gold nanoparticles were injected through the catheter placed in the auricular vein at 1 ml s^{-1}. After the last imaging session, animals were euthanized using a lethal dose of dolethal (Vetoquinol, Kontichsesteenweg, Aartselaar, Belgium). Specific organs were removed and prepared for gold content analysis using ICP-OES for comparison with SPCCT-based quantification of gold.

Images were acquired on the day of injection (D1), one week (W1), one month (M1) and six months later (M6). Imaging was performed at three time points on the day of injection, *i.e.* before injection (T0), 30–45 seconds (T1) and 7–8 minutes (T2) after injection of AuNPs, with images acquired at the level of the heart, liver, spleen, kidney, urinary cavity and brain. The images were acquired in the same organs at W1, M1 and M6 without additional injection of gold nanoparticles. A whole body scan was performed at the M6 time point. SPCCT images were acquired using the same scan parameters as used for the phantom scan.

Image processing

Axially acquired conventional CT images, water and gold images were analyzed using ImageJ software.[54] The attenuation values in HU were recorded from one slice, and the concentrations of gold (mg ml^{-1}) were recorded from an average of eight adjacent slice measurements, by manually drawing regions of interest (ROIs) in all rabbits for the imaged organs: thoracic aorta, myocardium, liver, spleen, left kidney and/or right kidney, bladder, paravertebral muscle, adipose tissue, bone marrow and brain. All ROIs were manually traced in the organs of interest by a senior radiologist (SSM, 6 years of experience) on the conventional images prior to retrieval of the gold concentrations per organ to avoid operator bias and then automatically copied on the gold images.

Inductively coupled plasma-optical emission spectrometry (ICP-OES)

Ex vivo analysis of the biodistribution of the gold nanoparticles was done using ICP-OES (Spectro Genesis ICP) according to a protocol published elsewhere.[23] The organs taken from the sacrificed animals were weighed, minced into small pieces and then 1 g portions were digested using 800 μl of concentrated nitric acid at 75 °C for 16 hours. After digestion with nitric acid, 250 μl of concentrated hydrochloric acid was added to each sample and the samples were incubated at 37 °C for 3 hours. After this incubation, the final volume of each sample was made to 3.5 ml with DI water. The gold content in each sample was analyzed using ICP-OES, reporting concentrations in mg g^{-1}. The SPCCT, since the images acquired were volumes, reported gold content as mg ml^{-1}.

Transmission electron microscopy

Organs of interest (liver, spleen, bone marrow, kidney and brain) were harvested, cut into one millimeter cubes, prefixed in 2.5% glutaraldehyde and prepared for TEM analysis using a conventional method.[55] Sections were examined with a JEOL 1400JEM (Tokyo, Japan) transmission electron microscope equipped with an Orius 1000 camera and a Digital Micrograph.

Statistics

For phantom analysis, linear regression was used to assess correlation between the measured and the expected concentrations. For the *in vivo* study, the linear regression and paired *T*-test were used to assess correlation and difference respectively between the measured concentrations by SPCCT and the concentration determined by the gold standard ICP-OES. Bland–Altman analysis was performed for both experiments.

Acknowledgements

References

1 C. H. McCollough, S. Leng, L. Yu and J. G. Fletcher, *Radiology*, 2015, **276**, 637–653.

2 E. Roessl, B. Brendel, K.-J. Engel, J.-P. Schlomka, A. Thran and R. Proksa, *IEEE Trans. Med. Imaging*, 2011, **30**, 1678–1690.

3 J. P. Schlomka, E. Roessl, R. Dorscheid, S. Dill, G. Martens, T. Istel, C. Bäumer, C. Herrmann, R. Steadman, G. Zeitler, A. Livne and R. Proksa, *Phys. Med. Biol.*, 2008, **53**, 4031–4047.

4 S. Si-Mohamed, D. Bar-Ness, M. Sigovan, D. P. Cormode, P. Coulon, E. Coche, A. Vlassenbroek, G. Normand, L. Boussel and P. Douek, *Nucl. Instrum. Methods Phys. Res. Sect. Accel. Spectrometers Detect. Assoc. Equip.*, 2017, DOI: 10.1016/j.nima.2017.04.014.

5 A. de Vries, E. Roessl, E. Kneepkens, A. Thran, B. Brendel, G. Martens, R. Proska, K. Nicolay and H. Grüll, *Invest. Radiol.*, 2015, **50**, 297–304.

6 S. T. Cochran, *Curr. Allergy Asthma Rep.*, 2005, **5**, 28–31.

7 P. A. McCullough, A. Adam, C. R. Becker, C. Davidson, N. Lameire, F. Stacul, J. Tumlin and CIN Consensus Working Panel, *Am. J. Cardiol.*, 2006, **98**, 5K–13K.

8 D. P. Cormode, P. C. Naha and Z. A. Fayad, *Contrast Media Mol. Imaging*, 2014, **9**, 37–52.

9 Q.-Y. Cai, S. H. Kim, K. S. Choi, S. Y. Kim, S. J. Byun, K. W. Kim, S. H. Park, S. K. Juhng and K.-H. Yoon, *Invest. Radiol.*, 2007, **42**, 797–806.

10 A. Jakhmola, N. Anton and T. F. Vandamme, *Adv. Healthcare Mater.*, 2012, **1**, 413–431.

11 J. F. Hainfeld, D. N. Slatkin, T. M. Focella and H. M. Smilowitz, *Br. J. Radiol.*, 2006, **79**, 248–253.

12 P. C. Naha, P. Chhour and D. P. Cormode, *Toxicol. In Vitro*, 2015, **29**, 1445–1453.

13 W. E. Ghann, O. Aras, T. Fleiter and M.-C. Daniel, *Langmuir*, 2012, **28**, 10398–10408.

14 M. W. Galper, M. T. Saung, V. Fuster, E. Roessl, A. Thran, R. Proksa, Z. A. Fayad and D. P. Cormode, *Invest. Radiol.*, 2012, **47**, 475–481.

15 D. P. Clark, K. Ghaghada, E. J. Moding, D. G. Kirsch and C. T. Badea, *Phys. Med. Biol.*, 2013, **58**, 1683–1704.

16 D. P. Cormode, P. C. Naha and Z. A. Fayad, *Contrast Media Mol. Imaging*, 2014, **9**, 37–52.

17 D. Pan, C. O. Schirra, S. A. Wickline and G. M. Lanza, *Contrast Media Mol. Imaging*, 2014, **9**, 13–25.

18 D. P. Cormode, E. Roessl, A. Thran, T. Skajaa, R. E. Gordon, J.-P. Schlomka, V. Fuster, E. A. Fisher, W. J. M. Mulder, R. Proksa and Z. A. Fayad, *Radiology*, 2010, **256**, 774–782.

19 A. S. Thakor, J. Jokerst, C. Zavaleta, T. F. Massoud and S. S. Gambhir, *Nano Lett.*, 2011, **11**, 4029–4036.

20 H. Lusic and M. W. Grinstaff, *Chem. Rev.*, 2013, **113**(3), 1641–1666.

21 K. Weintraub, *Nature*, 2013, **495**, S14–S16.

22 D. Kim, S. Park, J. H. Lee, Y. Y. Jeong and S. Jon, *J. Am. Chem. Soc.*, 2007, **129**, 7661–7665.

23 P. C. Naha, K. C. Lau, J. C. Hsu, M. Hajfathalian, S. Mian, P. Chhour, L. Uppuluri, E. S. McDonald, A. D. A. Maidment and D. P. Cormode, *Nanoscale*, 2016, **8**, 13740–13754.

24 W. Ngwa, R. Kumar, S. Sridhar, H. Korideck, P. Zygmanski, R. A. Cormack, R. Berbeco and G. M. Makrigiorgos, *Nanomed.*, 2014, **9**, 1063–1082.

25 R. Popovtzer, A. Agrawal, N. A. Kotov, A. Popovtzer, J. Balter, T. E. Carey and R. Kopelman, *Nano Lett.*, 2008, **8**, 4593–4596.

26 K. Taguchi and J. S. Iwanczyk, *Med. Phys.*, 2013, **40**, 100901.

27 C. O. Schirra, B. Brendel, M. A. Anastasio and E. Roessl, *Contrast Media Mol. Imaging*, 2014, **9**, 62–70.

28 E. Roessl, B. Brendel, K.-J. Engel, J.-P. Schlomka, A. Thran and R. Proksa, *IEEE Trans. Med. Imaging*, 2011, **30**, 1678–1690.

29 J. S. Iwanczyk, E. Nygård, O. Meirav, J. Arenson, W. C. Barber, N. E. Hartsough, N. Malakhov and J. C. Wessel, *IEEE Trans. Nucl. Sci.*, 2009, **56**, 535–542.

30 E. Roessl and R. Proksa, *Phys. Med. Biol.*, 2007, **52**, 4679.

31 D. P. Cormode, E. Roessl, A. Thran, T. Skajaa, R. E. Gordon, J.-P. Schlomka, V. Fuster, E. A. Fisher, W. J. M. Mulder, R. Proksa and Z. A. Fayad, *Radiology*, 2010, **256**, 774–782.

32 A. de Vries, E. Roessl, E. Kneepkens, A. Thran, B. Brendel, G. Martens, R. Proska, K. Nicolay and H. Grüll, *Invest. Radiol.*, 2015, **50**, 297–304.

33 I. M. Blevis, A. Altman and Y. Berman, *et al.*, Introduction of Philips preclinical photon counting scanner and detector technology development, *Presented at the IEEE Nuclear Science Symposium and Medical Imaging Conference*, San Diego, Calif, October 31–November 7, 2015.

34 T. L. McGinnity, O. Dominguez, T. E. Curtis, P. D. Nallathamby, A. J. Hoffman and R. K. Roeder, *Nanoscale*, 2016, **8**, 13627–13637.

35 J. P. Schlomka, E. Roessl, R. Dorscheid, S. Dill, G. Martens, T. Istel, C. Bäumer, C. Herrmann, R. Steadman, G. Zeitler, A. Livne and R. Proksa, *Phys. Med. Biol.*, 2008, **53**, 4031–4047.

36 R. Grosjean, B. Sauer, R. M. Guerra, M. Daudon, A. Blum, J. Felblinger and J. Hubert, *Am. J. Roentgenol.*, 2008, **190**, 720–728.

37 K. T. Butterworth, J. R. Nicol, M. Ghita, S. Rosa, P. Chaudhary, C. K. McGarry, H. O. McCarthy, G. Jimenez-Sanchez, R. Bazzi, S. Roux, O. Tillement, J. A. Coulter and K. M. Prise, *Nanomed.*, 2016, **11**, 2035–2047.

38 G. Laurent, C. Bernhard, S. Dufort, G. Jiménez Sánchez, R. Bazzi, F. Boschetti, M. Moreau, T. H. Vu, B. Collin, A. Oudot, N. Herath, H. Requardt, S. Laurent, L. Vander Elst, R. Muller, M. Dutreix, M. Meyer, F. Brunotte, P. Perriat, F. Lux, O. Tillement, G. Le Duc, F. Denat and S. Roux, *Nanoscale*, 2016, **8**, 12054–12065.

39 H. S. Choi, W. Liu, P. Misra, E. Tanaka, J. P. Zimmer, B. Itty Ipe, M. G. Bawendi and J. V. Frangioni, *Nat. Biotechnol.*, 2007, **25**, 1165–1170.

40 E. Sadauskas, G. Danscher, M. Stoltenberg, U. Vogel, A. Larsen and H. Wallin, *Nanomedicine*, 2009, **5**, 162–169.

41 J. F. Hainfeld, D. N. Slatkin, T. M. Focella and H. M. Smilowitz, *Br. J. Radiol.*, 2006, **79**, 248–253.

42 D. P. Clark and C. T. Badea, *Phys. Med. Biol.*, 2014, **59**, 6445–6466.

43 J. J. Pouw, M. R. Grootendorst, R. Bezooijen, C. A. H. Klazen, W. I. De Bruin, J. M. Klaase, M. A. Hall-Craggs, M. Douek and B. Ten Haken, *Br. J. Radiol.*, 2015, **88**, 20150634.

44 M. K. Seale, O. A. Catalano, S. Saini, P. F. Hahn and D. V. Sahani, *RadioGraphics*, 2009, **29**, 1725–1748.

45 C. O. Schirra, A. Senpan, E. Roessl, A. Thran, A. J. Stacy, L. Wu, R. Proska and D. Pan, *J. Mater. Chem.*, 2012, **22**, 23071–23077.

46 D. Pan, E. Roessl, J.-P. Schlomka, S. D. Caruthers, A. Senpan, M. J. Scott, J. S. Allen, H. Zhang, G. Hu, P. J. Gaffney, E. T. Choi, V. Rasche, S. A. Wickline, R. Proksa and G. M. Lanza, *Angew. Chem., Int. Ed.*, 2010, **49**, 9635–9639.

47 D. Pan, C. O. Schirra, A. Senpan, A. H. Schmieder, A. J. Stacy, E. Roessl, A. Thran, S. A. Wickline, R. Proska and G. M. Lanza, *ACS Nano*, 2012, **6**, 3364–3370.

48 P. F. FitzGerald, R. E. Colborn, P. M. Edic, J. W. Lambert, A. S. Torres, P. J. Bonitatibus and B. M. Yeh, *Radiology*, 2016, **278**, 723–733.

49 P. J. Bonitatibus, A. S. Torres, B. Kandapallil, B. D. Lee, G. D. Goddard, R. E. Colborn and M. E. Marino, *ACS Nano*, 2012, **6**, 6650–6658.

50 A. L. Brown, P. C. Naha, V. Benavides-Montes, H. I. Litt, A. M. Goforth and D. P. Cormode, *Chem. Mater.*, 2014, **26**, 2266–2274.

51 S. Rathnayake, J. Mongan, A. S. Torres, R. Colborn, D.-W. Gao, B. M. Yeh and Y. Fu, *Contrast Media Mol. Imaging*, 2016, **11**, 254–261.

52 R. Steadman, C. Herrmann and A. Livne, *Nucl. Instrum. Methods Phys. Res., Sect. A*, 2017, **862**, 18–24.

53 F. Blasi, B. L. Oliveira, T. A. Rietz, N. J. Rotile, H. Day, P. C. Naha, D. P. Cormode, D. Izquierdo-Garcia, C. Catana and P. Caravan, *Arterioscler., Thromb., Vasc. Biol.*, 2015, **56**, 1088–1093.

54 C. A. Schneider, W. S. Rasband and K. W. Eliceiri, *Nat. Methods*, 2012, **9**, 671–675.

55 D. Horak, M. Babic, P. Jendelová, V. Herynek, M. Trchová, Z. Pientka, E. Pollert, M. Hájek and E. Syková, *Bioconjugate Chem.*, 2007, **18**, 635–644.